

Pulsation models for the $0.26 M_{\odot}$ star mimicking RR Lyrae pulsator. Model survey for the new class of variable stars

R. Smolec,^{1*} G. Pietrzyński,^{2,3} D. Graczyk,² B. Pilecki,^{2,3} W. Gieren,² I. Thompson,⁴
K. Stępień,³ P. Karczmarek,³ P. Konorski,³ M. Górski,³ K. Suchomska,³ G. Bono,^{5,6}
P. G. Prada Moroni^{7,8} and N. Nardetto⁹

¹Copernicus Astronomical Centre, Polish Academy of Sciences, Bartycka 18, 00-716 Warsaw, Poland

²Departamento de Astronomía, Universidad de Concepción, Casilla 160-C, Concepción, Chile

³Warsaw University Observatory, Al. Ujazdowskie 4, 00-478 Warsaw, Poland

⁴Carnegie Observatories, 813 Santa Barbara Street, Pasadena, CA 91101-1292, USA

⁵Dipartimento di Fisica, Università di Roma Tor Vergata, via della Ricerca Scientifica 1, I-00133 Rome, Italy

⁶INAF – Osservatorio Astronomico di Roma, Via Frascati 33, I-00040 Monte Porzio Catone, Italy

⁷Dipartimento di Fisica ‘E. Fermi’, Università di Pisa, Largo B. Pontecorvo 3, I-56127 Pisa, Italy

⁸INFN, Sezione di Pisa, Largo B. Pontecorvo 3, I-56127 Pisa, Italy

⁹Laboratoire Lagrange, UMR7293, UNS/CNRS/OCA, F-06300 Nice, France

Accepted 2012 October 18. Received 2012 October 17; in original form 2012 September 20

ABSTRACT

We present non-linear hydrodynamic pulsation models for OGLE-BLG-RRLYR-02792 – a $0.26 M_{\odot}$ pulsator, component of the eclipsing binary system, analysed recently by Pietrzyński et al. The star’s light and radial velocity curves mimic that of classical RR Lyrae stars, except for the bump in the middle of the ascending branch of the radial velocity curve. We show that the bump is caused by the 2:1 resonance between the fundamental mode and the second overtone – the same mechanism that causes the Hertzsprung bump progression in classical Cepheids. The models allow us to constrain the parameters of the star, in particular to estimate its absolute luminosity ($\approx 33 L_{\odot}$) and effective temperature (≈ 6970 K, close to the blue edge of the instability strip).

We conduct a model survey for the new class of low-mass pulsators similar to OGLE-BLG-RRLYR-02792 – products of evolution in the binary systems. We compute a grid of models with masses corresponding to half (or less) of the typical mass of RR Lyrae variable, $0.20 \leq M \leq 0.30 M_{\odot}$, and discuss the properties of the resulting light and radial velocity curves. Resonant bump progression is clear and may be used to distinguish such stars from classical RR Lyrae stars. We present the Fourier decomposition parameters for the modelled light and radial velocity curves. The expected values of the φ_{31} Fourier phase for the light curves differ significantly from that observed in RR Lyrae stars, which is another discriminant of the new class.

Key words: hydrodynamics – methods: numerical – binaries: eclipsing – stars: oscillations – stars: variables: RR Lyrae.

1 INTRODUCTION

OGLE-BLG-RRLYR-02792 (below shortened to RRLYR-02792) is a large amplitude, single-periodic ($P_0 \approx 0.6275$ d) pulsator, component of a physical, well-detached, double-lined eclipsing binary system discovered in the Galactic bulge by the Optical Gravitational Lensing Experiment (OGLE) survey (Soszyński et al. 2011)

and analysed in detail in the course of the Araucaria project by Pietrzyński et al. (2012). Disentangled *I*-band light curve and radial velocity curve are presented in Fig. 1. The pulsation period and shape of the light curve place the star among classical RR Lyrae stars pulsating in the fundamental mode (RRab stars), which is clear from the analysis of the Fourier decomposition parameters, amplitude ratios, R_{k1} , and Fourier phases, φ_{k1} . They are constructed through the fit of the Fourier series to the data, i.e.

$$m_I = A_0 + \sum_k A_k \sin(k\omega t + \varphi_k), \quad (1)$$

*E-mail: smolec@camk.edu.pl

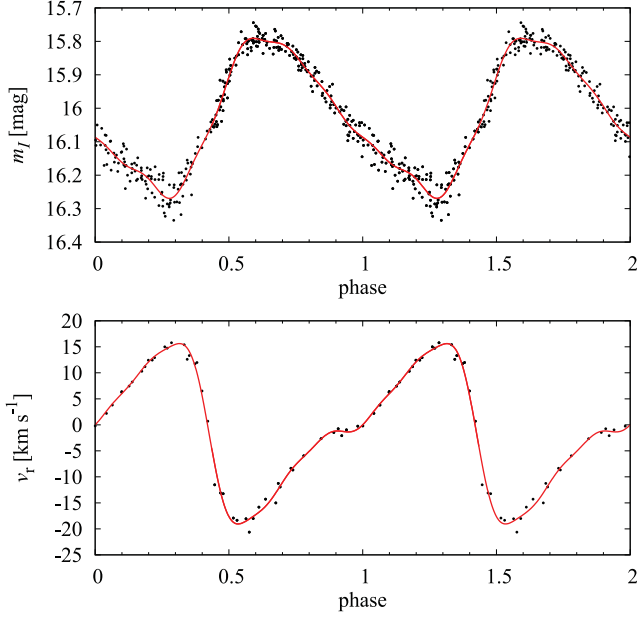


Figure 1. Disentangled I -band light curve (top) and radial velocity curve (bottom) for RRLYR-02792 (the BEP). Solid lines represent the 10th (light curve) and sixth (radial velocity curve) order Fourier fits to the data. Fourier decomposition parameters are given in Table 1. Note that we use an observers' convention in the plot of radial velocity curve, i.e. negative values correspond to expansion.

Table 1. Fourier decomposition parameters for the I -band light curve and radial velocity (RV) curve of RRLYR-02792 (the BEP, sine decomposition). Standard errors are given in the parentheses. In the last line, the peak-to-peak amplitude, A , is given.

	I -band	RV
A_1 (mag) (km s^{-1})	0.218(2)	13.46(27)
R_{21}	0.232(12)	0.526(27)
R_{31}	0.066(11)	0.160(21)
φ_{21} (rad)	2.93(5)	3.11(6)
φ_{31} (rad)	0.34(17)	-0.17(15)
A (mag) (km s^{-1})	0.486	34.67

and then,

$$R_{k1} = A_k/A_1, \quad \varphi_{k1} = \varphi_k - k\varphi_1, \quad (2)$$

where $\omega = 2\pi/P$ is pulsation frequency. As computed by Pietrzyński et al. (2012), the pulsation period decreases with the rate of $(8.4 \pm 2.6) \times 10^{-6} \text{ d yr}^{-1}$. Here we adopt the mean pulsation period derived from the I -band photometry, which spans nearly 10 years, $P_0 = 0.627527 \text{ d}$. Fourier decomposition parameters of RRLYR-02792 are given in Table 1 and plotted in Fig. 2, along with the OGLE data for thousands of RRab stars from the Galactic bulge (Soszyński et al. 2011). Note that the Fourier phases from the OGLE catalogue, given in the cosine convention, were shifted to match the sine convention (equation 1) that we consistently use in this paper (for both the light and radial velocity curves).¹ Fourier phases of RRLYR-02792 fit the typical values of RR Lyrae stars very well. Amplitude ratios are low, but fit the tail well visible in the progression for RRab stars between $P_0 = 0.6$ and 0.65 d .

¹ $\varphi_{21}^{(\text{sine})} = \varphi_{21}^{(\text{cosine})} - \pi/2$, $\varphi_{31}^{(\text{sine})} = \varphi_{31}^{(\text{cosine})} - \pi$.

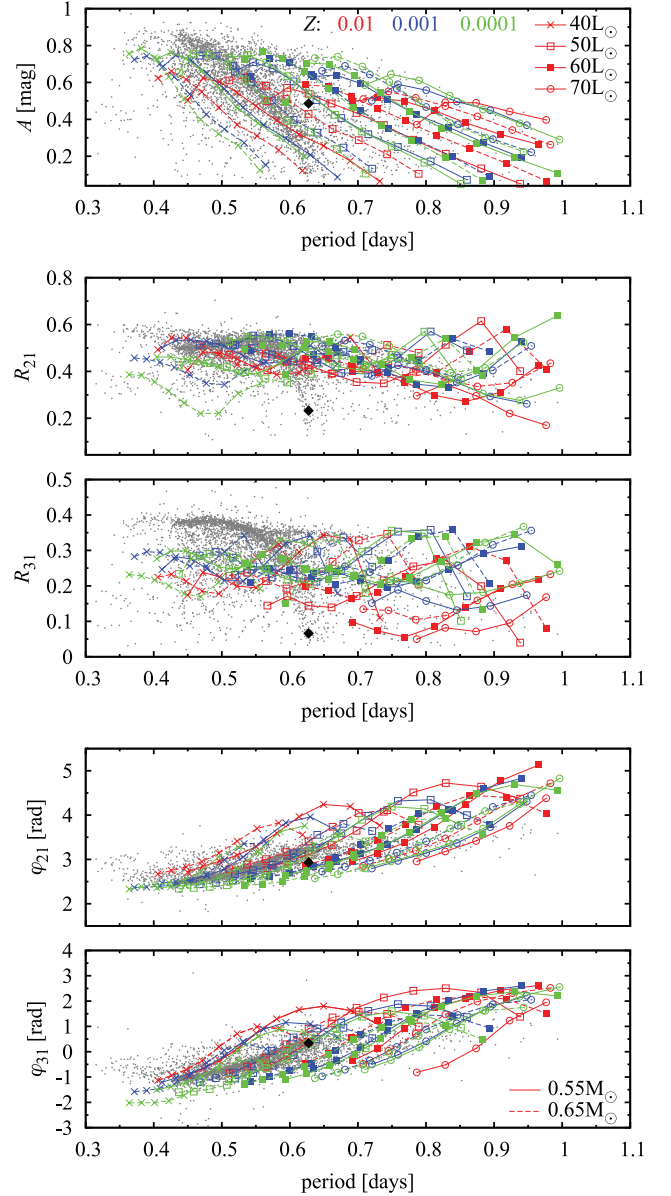


Figure 2. Peak-to-peak amplitude, A , and Fourier decomposition parameters for the I -band light curves of the Galactic bulge RR Lyrae stars of the OGLE survey (grey dots, each third plotted; Soszyński et al. 2011), RRLYR-02792 (the BEP, black diamond) and hydrodynamic models adopting convective parameters of set S1 (lines, see the keys in the top and bottom panels).

Surprisingly, the dynamical mass of RRLYR-02792 derived by Pietrzyński et al. (2012) is very low, $M = 0.261 \pm 0.015 M_{\odot}$, which is roughly two times smaller than the typical mass of the RR Lyrae star. It is too low to initiate the helium burning. As discussed by Pietrzyński et al. (2012), the star is a result of mass transfer in the binary system. Other parameters of RRLYR-02792 relevant for this study and derived by Pietrzyński et al. (2012) are radius, $R = 4.24 \pm 0.24 R_{\odot}$, and estimate of the effective temperature, $T_{\text{eff}} = 7320 \pm 160 \text{ K}$ (rough estimate based on the assumed 5000 K temperature of the secondary $1.67 M_{\odot}$ giant component and temperature ratio derived from the analysis of the light curve). Corresponding absolute luminosity may be estimated to be $L = 46.2 \pm 9.3 L_{\odot}$. No metallicity determination is available for RRLYR-02792.

RRLYR-02792 is a new member of a class of pulsators, for which mass transfer associated with binary evolution has significant effect on their pulsation properties. We will call such stars binary evolution pulsators (BEPs) and we will call the RRLYR-02792 the BEP. Other well-known examples of the class are hot subdwarf pulsators, members of eclipsing binary systems (see For et al. 2010). We also note that BEP may be a single object that went through binary evolution in the past, and was ejected from the binary because of, e.g., tidal interactions in the globular cluster.

In this paper, we present the first pulsation calculations for the BEP, both linear and non-linear, full-amplitude models. Nearly exact fit of the light and radial velocity curves is possible, which allows us to constrain the stellar parameters and provides an insight into the pulsation dynamics of the star (Section 3). We also present a non-linear model survey with parameters of the models corresponding to the expected parameters of the members of the new class, i.e. with masses two to three times smaller than typically assumed for RR Lyrae stars (Section 4). The main goal is to provide the criteria to distinguish the BEPs from classical RR Lyrae stars, for which binary nature cannot be inferred directly because of too low inclination angle. In this case, we only see the light/radial velocity curve of a pulsating component, which, as in the case of the BEP, may strongly mimic the typical curve of RR Lyrae pulsator.

2 NUMERICAL METHODS

All our models are computed with the convective pulsation codes described in detail by Smolec & Moskalik (2008). These are static model builder, linear non-adiabatic code and non-linear direct time-integration hydrodynamic code. The codes are Lagrangian. Radiative transfer is treated with a simple diffusion approximation. For the convective energy transport, we use the time-dependent, turbulent convection model of Kuhfuß (1986). It is a simple 1D, one-equation formulation that contains several dimensionless scaling parameters. These are the mixing-length parameter, α , and parameters scaling the turbulent fluxes and the terms that drive/damp the turbulent energy: α_p (turbulent pressure), α_m (eddy-viscous dissipation), α_c (convective heat flux), α_t (kinetic turbulent energy flux), α_s (buoyant driving), α_d (turbulent dissipation) and γ_r (radiative cooling). Theory provides no guidance for their values. For α_s , α_c , α_d and γ_r , values which result from comparison of the static time-independent version of the model with the mixing length theory are in use (see Table 2 caption). In practice, the values of convective parameters are calibrated to match as many observational constraints as possible. Slightly different values are necessary for modelling different groups of stars, e.g. Cepheids and RR Lyrae stars of different stellar systems. It makes the modelling of BEPs particularly difficult. The only known member of the class, the BEP, provides very little

Table 2. Convective parameters adopted in the models. Parameters α_s , α_c , α_d , α_p and γ_r are given in the units of standard values ($\alpha_s = \alpha_c = 1/2\sqrt{2/3}$, $\alpha_d = 8/3\sqrt{2/3}$, $\alpha_p = 2/3$ and $\gamma_r = 2\sqrt{3}$; see Smolec & Moskalik 2008, for details). Only first three sets of parameters were used in non-linear computations.

Set	α	α_m	α_s	α_c	α_d	α_p	α_t	γ_r
S1	1.5	0.4	1.0	1.0	1.0	0.0	0.0	0.0
S2	1.5	0.6	1.0	1.0	1.0	0.0	0.0	1.0
S3	1.5	0.2	1.0	1.0	1.0	0.0	0.0	0.0
S4	1.5	0.6	1.0	1.0	1.0	1.0	0.01	0.0

constraints on the models. Consequently, several sets of values of convective parameters need to be considered (Table 2). As a first guess, we adopt the parameters that well reproduce the observed properties of the Galactic bulge RR Lyrae stars, in particular the Fourier parameters of the *I*-band light curves. In Fig. 2, we compare the computed Fourier parameters for models adopting convective parameters of set S1 and assuming typical parameters of RR Lyrae stars (masses 0.55 and 0.65 M_\odot , luminosities: 40–70 L_\odot , metallicities, Z : 0.01, 0.001 and 0.0001) with OGLE observations. We get a good agreement for amplitudes, Fourier phases and R_{21} ratio, and somewhat too low model values for R_{31} . Similar agreement (with much better match of R_{31}) is obtained for models of set S2, which include the effects of radiative cooling. In set S3, the convective parameters are the same as in set S1, except eddy viscosity which is lower. Consequently, we expect higher pulsation amplitudes in models adopting parameters of set S3. In linear model survey, we also consider set S4, in which effects of turbulent pressure are turned on. Inclusion of turbulent pressure in non-linear models leads to long-lasting integration and convergence difficulties for some models. Consequently, in this first non-linear model survey for BEPs, we neglect the effects of turbulent pressure and consider models of sets S1, S2 and S3, only.

Our models are chemically homogeneous, non-rotating, envelope models. They consist of 150 mass shells extending down to 2×10^6 K. It is a standard depth in modelling the Cepheid and RR Lyrae pulsation. It is deep enough to cover the region relevant for κ mechanism driven pulsation but too shallow to enter the inhomogeneous hydrogen-burning shell region. In order to capture and resolve the thin hydrogen ionization region, the anchor zone of temperature equal to 11 000 K is located 40 zones below the surface. Non-linear model integration is conducted till the limit cycle pulsation (single-periodic, full-amplitude pulsation) is reached, which requires computation of 1000 up to 5000 pulsation cycles. Each pulsation cycle is covered with 600 time-steps. The bolometric light curves are transformed to the *I* band through the static Kurucz (2005) atmosphere models.² Projection factor for the BEP is unknown. We scaled the model velocity curves by projection factor used for classical RR Lyrae pulsators, i.e. $p = 1.38$ (Fernley 1994).

The chemical structure of the star is subject of uncertainty. No metallicity determination is available. Also, no realistic evolutionary computations exist for this type of binary evolution. Significant fraction of the envelope was removed during the evolution. Pulsation is driven in the outermost layers which, although very extended, contain only a fraction of per cent of the total stellar mass (typically below 1 per cent in our models). In this study, we assume that the outer shell has preserved the standard chemical composition typical for Population II stars, i.e. $X = 0.76$ and $Z = 0.01$ – 0.0001 . We also compute model sequences with $X = 0.70$, which corresponds to higher helium content as in Population I stars. In all our models, we adopt the Opacity Project (OP) opacities (Seaton 2005) and solar mixture of Asplund et al. (2004).

3 PULSATION MODELS FOR THE BEP

In this section, we focus on modelling the observed properties of the BEP. We first conduct a linear model survey and discuss properties of the static models (Section 3.1). Next, we focus on non-linear modelling of the *I*-band light curve and radial velocity curve of the BEP (Section 3.2).

² <http://kurucz.harvard.edu/>

3.1 Linear model survey

The models are computed along horizontal stripes of constant luminosity ($L = 16\text{--}40 L_{\odot}$, step $2 L_{\odot}$) and with 100 K step in effective temperature. We adopt $M = 0.26 M_{\odot}$ for all the models. Computed Hertzsprung–Russell (HR) diagrams for different sets of convective parameters and assuming different chemical compositions are plotted in Fig. 3. Except for model computations adopting convective parameters of set S2, first overtone is linearly damped in our models. The typical width of the fundamental mode instability strip is 1000 K and increases towards the higher luminosities.

Before we discuss the models appropriate for the BEP, we first discuss general properties of typical static model, as pulsation properties of BEPs were not studied so far. In Fig. 4, we plot results for a model located in the middle of the instability strip ($T_{\text{eff}} = 6500$ K, $L = 25 L_{\odot}$, marked with open circle in the top-left panel of Fig. 3). Its period is only slightly longer than the period of the BEP. The top panel shows the convective heat flux (solid line) and adiabatic temperature gradient (dashed line). In the middle panel of Fig. 4, we plot the logarithm of Rosseland opacity (solid line) and its logarithmic temperature derivative (dashed line) – crucial quantities for studying the pulsation driving. The metal, helium and hydrogen opacity bumps are marked with labels. In the bottom panel, the work integrands are plotted – total with the solid line and contribution of eddy-viscous work with the dashed line. Pulsation driving occurs in regions with positive work integrand. Eddy viscosity always damps the pulsation and its contribution is negative. Model properties are very similar to the properties of classical RR Lyrae

models (e.g. Stellingwerf 1982). It is clear that pulsation is driven through the κ mechanism working in the hydrogen–helium ionization zone. We note a significant contribution from the hydrogen ionization region. The main envelope convection zone is associated with the hydrogen–helium (He I–H) ionization region. The second, less effective convective region develops deeper at the He II ionization zone. All ionization regions are properly resolved in our models as the run of ∇_{ad} indicates.

In each panel of Fig. 3, we plot a line of constant fundamental mode period, $P_0 = 0.627527$ d. The dashed lines in Fig. 3 are lines of constant photospheric radius $R = 4.24 R_{\odot}$, with 1σ errors ($\pm 0.24 R_{\odot}$), which correspond to the values measured for the BEP. For models with mass corresponding to the measured mass of the BEP, these two lines (of constant $P_0 = 0.6275$ d and of constant $R = 4.24 R_{\odot}$) should roughly overlap (period–mean density relation), which is not the case for any of the considered model parameters. The lines are nearly parallel but shifted with respect to each other. The best agreement is obtained for models of the lowest metal abundance and for the models including the effects of turbulent pressure, which expands the model envelope (bottom right panel in Fig. 3). In this case, the difference is 1σ (at high L). For other models, the difference is larger; however, it is always smaller than 2σ . Hence, we treat this discrepancy as a warning sign and note that multiband photometric observations are necessary to derive the radius of the BEP more accurately (see also discussion in Section 5).

In the HR diagrams in Fig. 3, we also plot the loci of the 2:1 resonance between the fundamental mode and the second overtone, $P_2/P_0 = 0.5$ (dotted lines). This resonance causes the famous

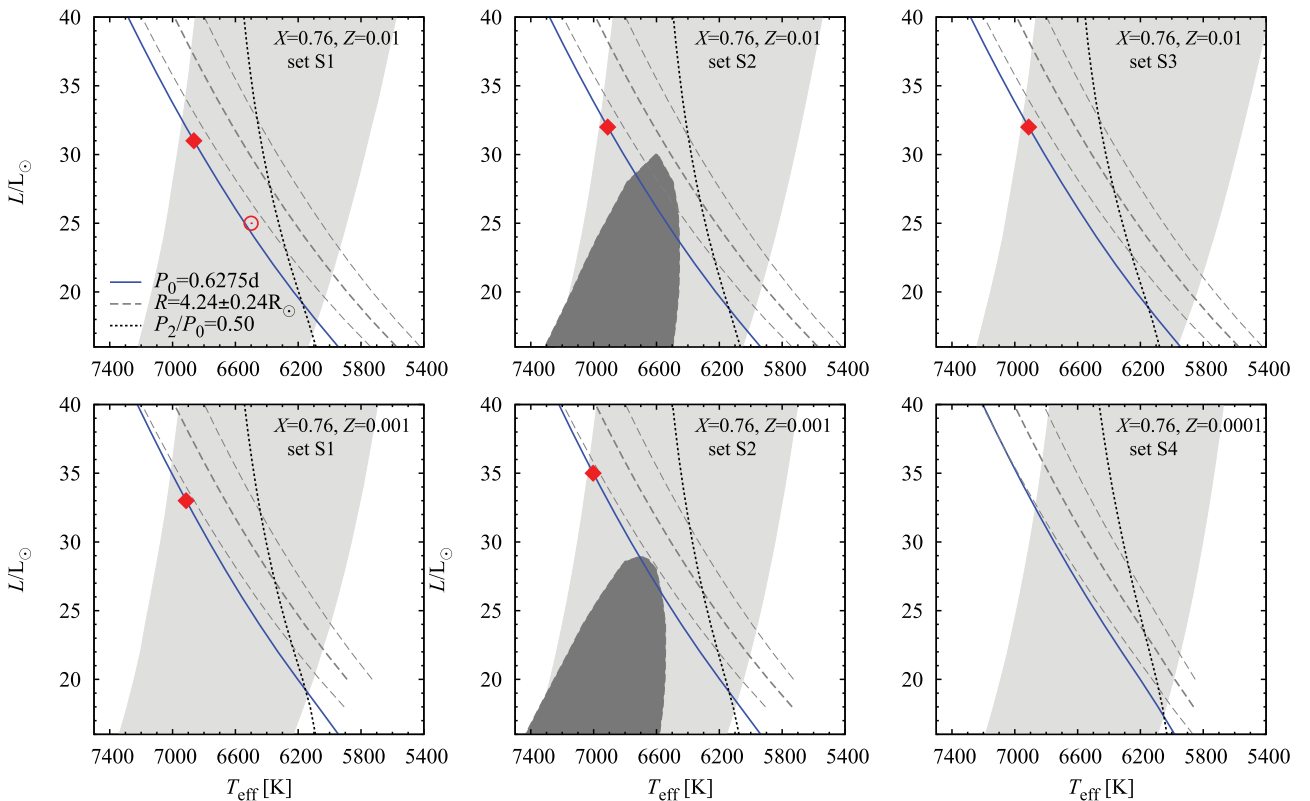


Figure 3. The HR diagrams for $0.26 M_{\odot}$ models adopting different values of convective parameters and different chemical compositions as indicated in the top-right part of each panel. Instability strips are indicated with grey-shaded areas (light grey for the fundamental mode, dark grey for the first overtone). Solid line is the line of constant fundamental mode period, $P_0 = 0.6275$ d. Long-dashed lines indicate the radius determination for the BEP (with 1σ errors) and dotted line shows the loci of the 2:1 resonance with the second overtone, $P_2/P_0 = 0.5$. Circle marks location of the static model from Fig. 4, and diamonds mark the location of the best matching models for the BEP (Section 3.2, Table 3).

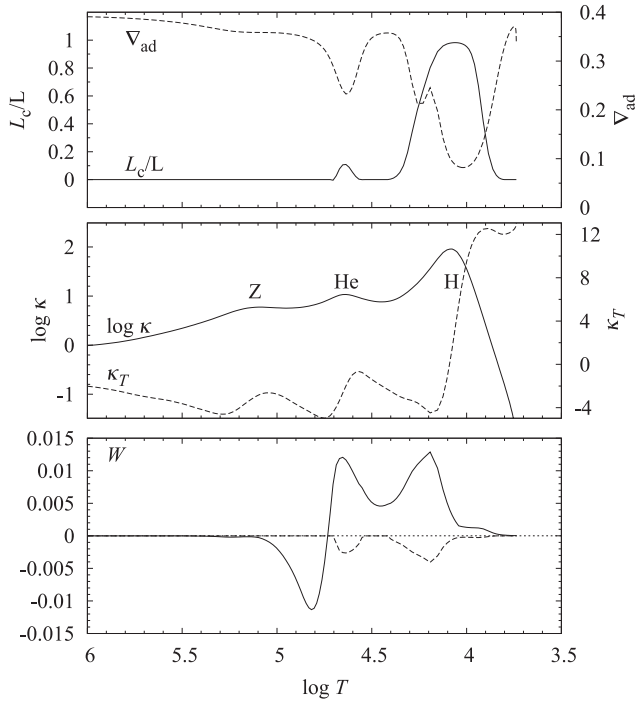


Figure 4. Properties of the exemplary static model with $M = 0.26 M_{\odot}$, $L = 25 L_{\odot}$ and $T_{\text{eff}} = 6500$ K (marked with circle in the top-left panel of Fig. 3). Top panel: convective heat flux (solid line) and adiabatic temperature gradient (dashed line); middle panel: logarithm of opacity (solid line) and its logarithmic temperature derivative (dashed line); bottom panel: work integrands, total (solid line) and eddy-viscous contribution (dashed line).

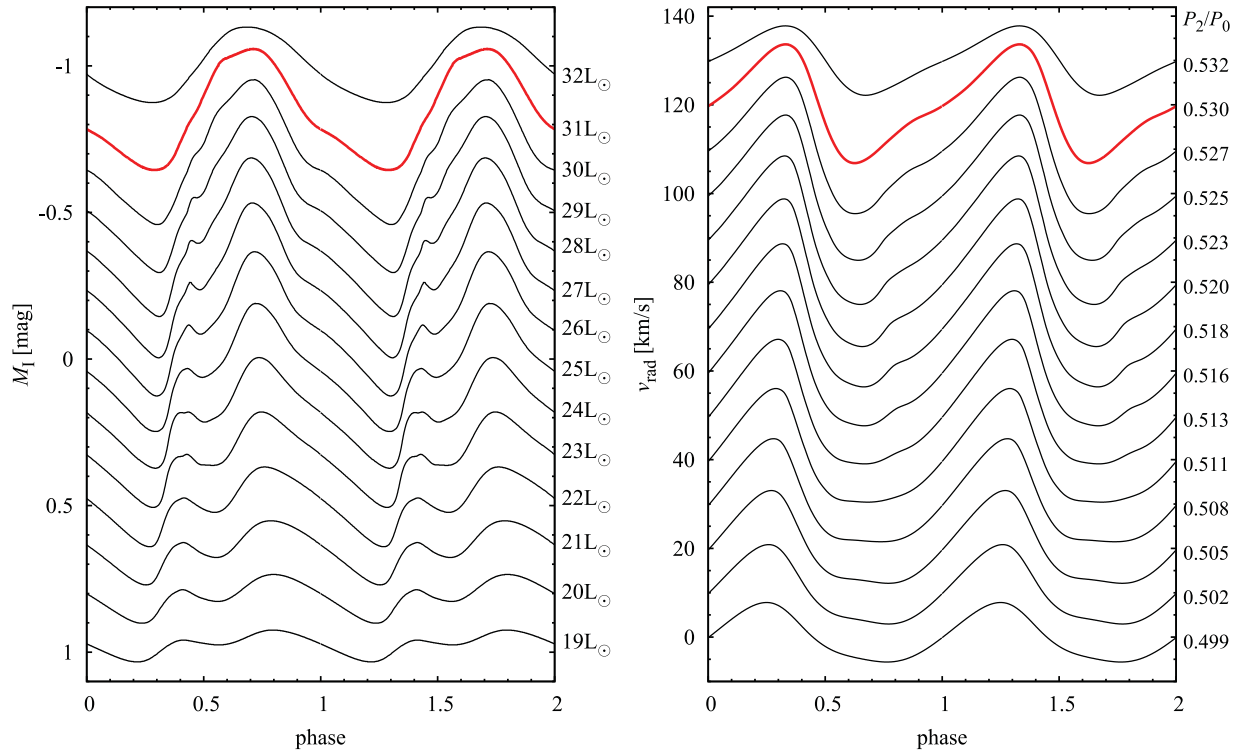


Figure 5. *I*-band light curves (left-hand panel) and radial velocity curves (right-hand panel, observers' convention, i.e. negative values correspond to envelope expansion) for hydrodynamic models of $0.26 M_{\odot}$ computed along a line of constant fundamental mode period corresponding to the pulsation period of the BEP. Models adopt convective parameters of set S1. For clarity, the consecutive light curves were shifted by 0.12 mag and radial velocity curves by 10 km s^{-1} . Velocity curves were scaled by constant projection factor, $p = 1.38$. Thick red lines indicate the best matching model for the BEP.

Hertzsprung bump progression in classical Cepheids pulsating in the fundamental mode (e.g. Simon & Schmidt 1976; Kovács & Buchler 1989; Buchler, Moskalik & Kovács 1990). In the discussed models, it lies well within the instability strip, independent of the model parameters (see also Fig. 9 for models with different mass). Our non-linear computations presented in the next sections show that this resonance strongly influences the pulsation of BEPs.

3.2 Non-linear model survey

The non-linear models for the BEP are computed along lines of constant fundamental mode period, $P_0 = 0.6275$ d. Models are labelled by their absolute luminosity, which increases in a step of $1 L_{\odot}$. All models have $M = 0.26 M_{\odot}$. The least luminous models are located at the red edge of the instability domain and, as luminosity increases, shift towards the blue (see Fig. 3). We computed six model sequences: with convective parameters of sets S1, S2 and S3, and with metallicities $Z = 0.01$ and 0.001 ($X = 0.76$) in each case. For models with convective parameters of set S3, we also computed two model sequences with $X = 0.70$ ($Z = 0.01$ and 0.001). In Fig. 5, we show a full set of the computed *I*-band light curves and radial velocity curves for models with convective parameters of set S1 and with $Z = 0.01$. At phase 0, the radius reaches its maximum value (velocity is equal to 0). The radial velocity curves have a usual triangular shape. One may note a systematic progression of the curve's shape as luminosity changes. For the lowest luminosity models, the velocity curves are more or less symmetrical; the descending branch is even slightly longer than the ascending branch for the model with $L = 19 L_{\odot}$. The velocity varies slowly at the phase of maximum expansion. For models with $L = 22\text{--}23 L_{\odot}$, the velocity

curve is nearly flat at this phase. As luminosity increases, a bump appears on the ascending branch (visible already for $L = 25 L_{\odot}$ at phase around 0.8), which moves upwards towards the phase of maximum radius ($L = 31 L_{\odot}$) and then vanishes ($L = 32 L_{\odot}$).

Considering the I -band light curves, at the lowest luminosities they differ significantly from the typical RR Lyrae curves. A pronounced bump is present on the ascending branch – two brightness maxima are observed during one pulsation cycle. As luminosity increases, the bump becomes less pronounced, turns into narrow standstill (28, 29 L_{\odot}) and vanishes. At highest luminosities, the light curves resemble those of typical RR Lyrae stars, except for less sharp light variation in the brightness maximum.

Described variation of the shape of radial velocity and I -band light curves suggests that the 2:1 resonance with the second overtone is influential here, and shapes the bump progression. It is not very pronounced because we consider a specific model sequences of constant period. It is clear from Fig. 3 that most of our models lie to the blue of the $P_2/P_0 = 0.5$ line and thus majority of models have $P_2/P_0 > 0.5$ – see exact values on the right-hand side of Fig. 5. In the case of bump progression observed, e.g., in classical Cepheids, which is caused by the same resonance, the shape of the light/radial velocity curves is affected by the resonance in a wide range of period ratios, $0.48 < P_2/P_0 < 0.54$. The position of the bump depends critically on the value of P_2/P_0 , as model computations indicate (Kovács & Buchler 1989; Buchler et al. 1990). For $P_2/P_0 > 0.5$, the bump is located on the ascending branch of the velocity curve, which is also the case in our models. The full bump progression in our models will be demonstrated in Section 4, where we consider models covering the full instability strip and thus probing the P_2/P_0 ratio in a wide range (Fig. 11).

It is clear that, among the models displayed in Fig. 5, these are the highest luminosity ones that reproduce the observations of the BEP best (cf. Fig. 1). In particular, the model for $L = 31 L_{\odot}$ (marked with thick red lines in Fig. 5) seems to be the best one. A more quantitative selection of the best models for the BEP is based on comparison of the observed and computed Fourier decomposition parameters of the lowest order, the amplitude A_1 , amplitude ratios, R_{21} and R_{31} , and Fourier phases, φ_{21} and φ_{31} , for both I -band and radial velocity curves. In Figs 6 and 7, we show such comparisons for specific Fourier parameter planes, i.e. φ_{21} – R_{21} and φ_{31} – R_{31} , and three sequences of models. We stress that periods of all the models match the period of the BEP. Models differ in luminosity (and effective temperature) – the least luminous model (and the coolest one) is marked with an open circle. Luminosity of the consecutive models in a sequence differs by $1 L_{\odot}$. Again, it is clear that these are the highest luminosity models that match the observations of the BEP best.

Yet another observable that can be compared with the models is the phase lag between the radial velocity curve and the light curve, defined as $\Delta\varphi_1 = \varphi_1^{\text{vel}} - \varphi_1^{\text{mag}}$ (Simon 1984). For the BEP, we get $\Delta\varphi_1 = 0.055 \pm 0.027$.³ Unfortunately, there are no phase lag determinations for classical RR Lyrae stars using the I -band light curves. With the V -band light curves, the mean phase lag for a sample of RR Lyrae stars is $\langle \Delta\varphi_1 \rangle = -0.19$ (Ogloza, Moskalik & Kanbur 2000). It is negative for all the stars used in the work of Ogloza et al. (2000)

³ Because of the pulsation period change, $\Delta\varphi_1$ was computed using the last 500 days of the OGLE-III photometry only. At the end of this span, the radial velocities were measured. The adopted pulsation period [$P = 0.627510(5)$ d] was derived from the photometry alone, but agrees well with the (less accurate) period derived from radial velocity measurements.

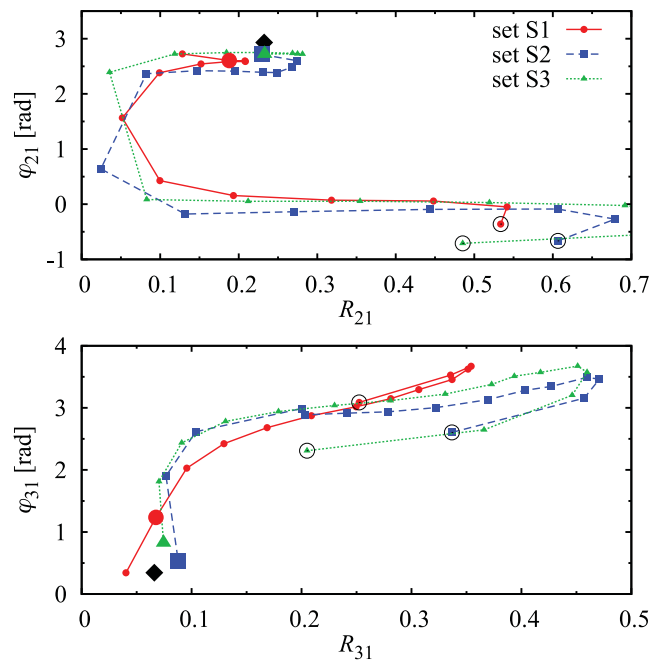


Figure 6. Plots of the Fourier parameters, φ_{21} versus R_{21} (top) and φ_{31} versus R_{31} (bottom) for the computed I -band light curves for three sequences of models of constant period (all models with $X = 0.76$ and $Z = 0.01$, but with different convective parameters, as indicated in the key). Open circle marks the first, lowest luminosity model in each sequence. Consecutive models differ by $1 L_{\odot}$. Larger symbols show the best matching models for the BEP (marked with diamond).

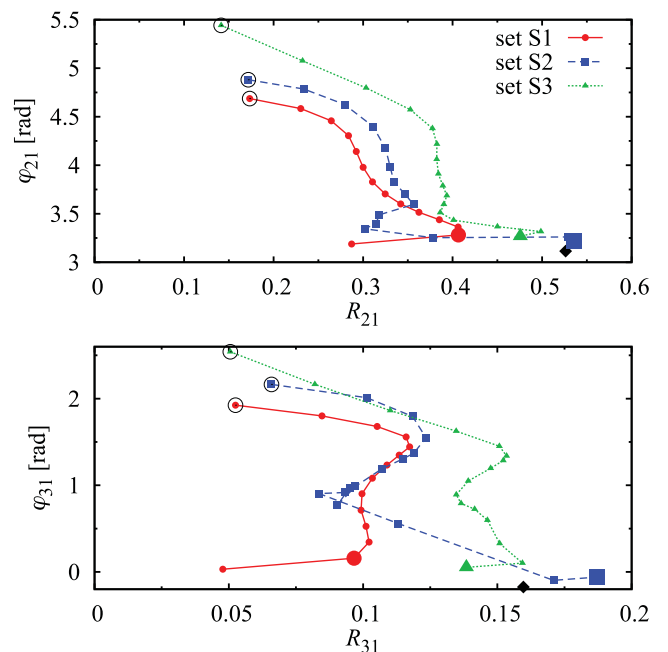


Figure 7. The same as Fig. 6, but for the radial velocity curves.

(Moskalik, private communication). Our models for classical RRab stars (displayed in Fig. 2) point, however, that phase lags computed using the I -band light curves are systematically larger than phase lags computed using the V -band light curves and may have both positive and negative values.

We now compute the offsets between the model and the observations in the Fourier parameter space, defined as

$$d = \sqrt{\sum_i (p_{i,\text{mod}} - p_{i,\text{obs}})^2 / p_{i,\text{obs}}^2}, \quad (3)$$

where p_i denotes one of the low-order Fourier parameters and amplitudes, $p_i \in \{A, R_{21}, R_{31}, \varphi_{21}, \varphi_{31}\}$, for our models ($p_{i,\text{mod}}$) and for the observed curves ($p_{i,\text{obs}}$, Table 1). Depending on the Fourier parameters used, several offsets may be constructed. At first, we consider three definitions of d . The first offset, d_2 , is computed in the 2D plane of the lowest order Fourier coefficients, φ_{21} – R_{21} (top panels of Figs 6 and 7). The second offset, d_4 , is constructed from all four low-order amplitude ratios and Fourier phases, and the third offset, d_5 , includes also the amplitude.

We note that for a given model sequence and for both the I -band and radial velocity curves the three offsets are minimized either for the same model or by models that differ by $1 L_\odot$. For example, for models adopting convective parameters of set S2 and $Z = 0.01$, all offsets for the I -band light curves and radial velocity curves are minimized in the model with $L = 32 L_\odot$, except d_4 for the radial velocity curves which is minimized in the model with $L = 31 L_\odot$. In the more complex case of models with convective parameters of set S1 (and $Z = 0.01$), d_4 and d_5 for the I -band light curves and d_2

for the radial velocity curves are minimized in the model with $L = 31 L_\odot$, while d_2 for the I -band light curves and d_4 and d_5 for the radial velocity curves are minimized in the model with $L = 30 L_\odot$.

For the final selection of the best model, we use the offset d_{all} constructed from all low-order Fourier decomposition parameters and amplitudes for both the I -band light curve and radial velocity curve (10 parameters). The model that minimizes d_{all} for a given model sequence is considered the best one. Properties of our best matching models for all considered model sequences are given in Table 3. In the last row, we provide the value of d_{all} . In the HR diagrams in Fig. 3, location of the best models is indicated with diamonds (in relevant panels). In Figs 6 and 7, the best models are marked with larger symbols. In Fig. 8, the light and radial velocity curves for our best models for the BEP are compared with observations. The light curves were shifted vertically so the mean brightness is zero. All the curves were phased in the same way – phase 0 corresponds to the maximum radii (radial velocity goes through 0). No other shifts were applied to the curves (except the vertical shift between consecutive models applied for clarity).

Analysis of Table 3 and Figs 3, 6, 7 and 8 allows us to draw some interesting conclusions.

(i) All the best-fitting models are located close to the blue edge of the instability strip (Fig. 3). The effective temperatures and

Table 3. Properties of the best hydrodynamic models for the BEP.

Set	S1		S2		S3			
	0.76/0.01	0.76/0.001	0.76/0.01	0.76/0.001	0.76/0.01	0.76/0.001	0.70/0.01	0.70/0.001
L/L_\odot	31	33	32	35	32	34	33	36
T_{eff} (K)	6864.2	6913.8	6910.5	7003.0	6911.4	6957.3	6966.7	7053.6
R/R_\odot	3.88	3.94	3.88	3.95	3.88	3.95	3.88	3.96
P_2/P_0	0.530	0.537	0.536	0.545	0.532	0.539	0.532	0.542
$\Delta\varphi_1$	−0.14	−0.11	−0.16	−0.14	−0.13	−0.03	−0.07	−0.06
d_{all}	0.597	0.421	0.382	0.742	0.290	0.630	0.200	0.227

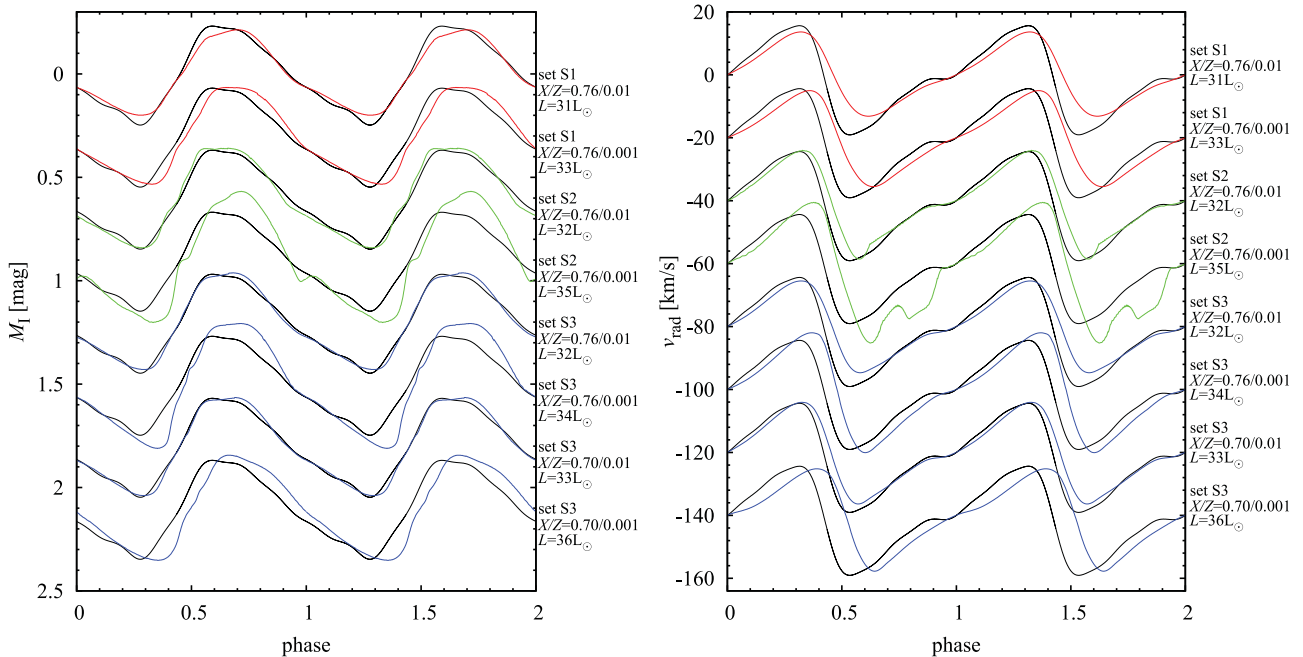


Figure 8. I -band (left-hand panel) and radial velocity (right-hand panel) curves for hydrodynamic models reproducing the observations of the BEP (black solid line, Fourier fit from Fig. 1) best. Models adopting convective parameters of sets S1, S2 and S3 are plotted with red, green and blue lines, respectively.

absolute luminosities lie in a narrow ranges of $\sim 6850\text{--}7050\text{ K}$ and $31\text{--}36 L_{\odot}$, respectively. More metal-rich models ($Z = 0.01$) are slightly ($50\text{--}100\text{ K}$) cooler and less luminous ($2\text{--}3 L_{\odot}$) than metal-poor models ($Z = 0.001$).

(ii) Radius depends on metallicity and is equal to $\approx 3.88 R_{\odot}$ for $Z = 0.01$ and $\approx 3.95 R_{\odot}$ for $Z = 0.001$.

(iii) Considering the *I*-band light curves (left-hand panel of Fig. 8), clearly the best fit to the observed light curve is obtained for models with convective parameters of set S3 and with $X = 0.70$ (for both metallicities, bottom two curves in Fig. 8). These are the models with the lowest value of d_{all} . A slightly worse fit is obtained for models with $X = 0.76$. Among these models, the best ones are those with convective parameters of sets S2 and S3 and with the higher metallicity ($Z = 0.01$, third and fifth curves from top in Fig. 8). For all these models, the radial velocity curves well reproduce the observed curve; in particular, a bump on the ascending branch is present, although less pronounced than in observations. We conclude that chemical composition typical for Population I stars ($X = 0.70$) seems more appropriate for the BEP (see discussion in Section 5).

(iv) For the lower metallicity models ($Z = 0.001$), a phase shift between the model and the observed light curves is apparent for models of all three sets of convective parameters (left-hand panel in Fig. 8). A minimum brightness in these models follows the observed minimum by $\approx 0.1\text{--}0.15$ pulsation cycle. The shift is also present in the case of the radial velocity curves, for all the models. A phase of maximum expansion velocity in our models occurs later than is observed. Again the difference is slightly larger for the lower metallicity models. To explain these phase shifts, we first note that we defined phase 0 as the phase of maximum radius. It is determined with the help of the radial velocity, which changes the sign. At around this phase, a bump is present in the radial velocity curves, which manifests itself as a slower (less steep) variation of the radial velocity. Thus, its exact location may influence our phasing of the model curves. The location of the bump depends on the P_2/P_0 period ratio which is a function of metallicity, as is evident from an analysis of the values given in Table 3. At lower metallicity, the P_2/P_0 ratio becomes larger and the bump moves up the ascending branch of the radial velocity curve. The second effect is a systematic difference between the observed and the computed phase lag between the radial velocity curves and the light curves. Indeed, the phase lag of the BEP is positive and equal to $\Delta\varphi_1 = 0.055$, while the phase lags for all our models (Table 3) are systematically smaller and negative. A significantly better agreement is obtained for models with higher helium content, i.e. with $X = 0.70$. We also note that in spite of the model phase lags being all negative, the phase of maximum expansion velocity always precedes the phase of maximum brightness, just as in the case of the BEP. The negative value of $\Delta\varphi_1$ results from the highly non-linear shape of the light and radial velocity curves.

(v) The model for the BEP that reproduces both the light and radial velocity variation best (has the lowest value of d_{all}) is the model with convective parameters of set S3 and with chemical composition of Population I stars ($X = 0.70$, $Z = 0.01$). Its absolute luminosity is $33 L_{\odot}$ and effective temperature is $\approx 6970\text{ K}$. Among the models with chemical composition corresponding to Population II stars, the best two models (with convective parameters of sets S2 and S3) have the same metallicity ($Z = 0.01$), luminosity ($L = 32 L_{\odot}$) and nearly the same effective temperature ($\approx 6910\text{ K}$). All our best matching models have very similar P_2/P_0 ratios, in agreement with interpretation that the bump is caused by the 2:1 resonance between the fundamental mode and the second overtone.

4 NON-LINEAR MODEL SURVEY FOR BEPs

At first, the BEP was recognized as a classical RR Lyrae star – its light variation and radial velocity curves mimic that observed in RR Lyrae stars pulsating in the fundamental mode. Only its presence in the eclipsing binary system allowed us to determine its mass and to reveal its true nature. Its mass is only half the typical RR Lyrae mass, too low to ignite helium. It cannot be a classical RR Lyrae star; it is a product of mass transfer during the binary evolution. The incidence rate of such stars estimated by Pietrzyński et al. (2012) is only 2 per cent and only a fraction may be discovered through eclipses. Majority of such binaries are expected to be non-eclipsing systems. Consequently, direct estimate of mass of the pulsating component will not be possible. Then, the shape of the light/radial velocity curve may mimic that of RRab star, as it is the case for the BEP, and lead to wrong interpretation. The goal of this section is to conduct a large model survey of the light and radial velocity curves of BEPs, to check how to distinguish these stars from classical RRab stars and to check whether the case of the BEP – RR Lyrae impostor – is a rule or an exception.

We consider model sequences with three different masses corresponding to one-third – one-half the typical RR Lyrae mass, 0.2, 0.26 (mass of the BEP) and $0.3 M_{\odot}$, and with different absolute luminosities, 20, 25, 30, 35 and $40 L_{\odot}$. Models are computed along horizontal stripes of constant luminosity with a step of 100 K in effective temperature. Chemical composition is the same in all our models, $X = 0.76$ and $Z = 0.01$. Full model survey was computed adopting convective parameters of set S1. In addition, for $0.26 M_{\odot}$ we have computed model sequences adopting convective parameters of sets S2 and S3.

In Fig. 9, we present the HR diagrams for models with $M = 0.20 M_{\odot}$ (top panel) and $M = 0.30 M_{\odot}$ (bottom panel), adopting convective parameters of set S1. For $M = 0.26 M_{\odot}$, the HR diagram is plotted in the top-left panel in Fig. 3. For the highest considered mass, the first overtone instability strip appears at the lowest luminosities. The models cover a wide period range from 0.3 to 1.5 d. We focus our attention on models with P_0 below 1 d, as in RRab stars. As discussed in the previous section, the 2:1 resonance is expected to shape the light and radial velocity curves of BEPs. For all considered masses, its loci (thick dotted lines in Figs 9 and 3) cross the instability strip at fundamental mode periods between 0.6 and 1 d.

An analysis of the light and radial velocity curves and of the corresponding Fourier decomposition parameters clearly show that indeed the 2:1 resonance with the second overtone causes the progression of the light and radial velocity curve's shape. This is illustrated based on model sequences with $M = 0.26 M_{\odot}$ (and different luminosities) and adopting convective parameters of set S1. The bump progression, akin to that observed in classical Cepheids, is best visible for radial velocity curves. The amplitude and the lowest order Fourier decomposition parameters are plotted in Fig. 10 for model sequences with different luminosities. The Fourier parameters are plotted versus the P_2/P_0 period ratio. The progression of the Fourier coefficients clearly correlates with P_2/P_0 ratio and resembles very well the results obtained for classical Cepheid models (e.g. Buchler et al. 1990) and predictions based on analysis of amplitude equations for the 2:1 resonance (Kovács & Buchler 1989). A clear drop in the pulsation amplitude is observed, followed by the decrease and minimum of the R_{21} ratio at somewhat larger values of P_2/P_0 . In the case of the Fourier phase, a bell shape is apparent. The ascending part of the bell follows a universal progression – φ_{21} is a function of P_2/P_0 only (for $P_2/P_0 > 0.52$). The value of P_2/P_0 at

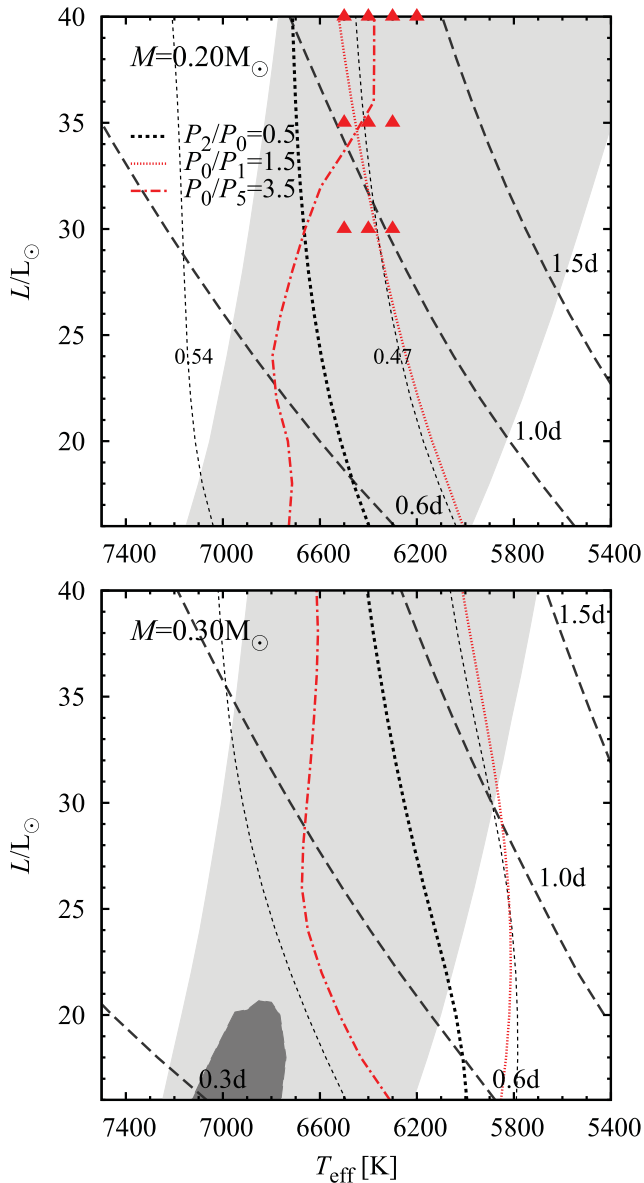


Figure 9. The HR diagrams for $0.20 M_{\odot}$ (top panel) and $0.30 M_{\odot}$ (bottom panel) models of set S1 and with $X = 0.76$ and $Z = 0.01$. Long-dashed lines are lines of constant fundamental mode period (0.3, 0.6, 1.0 and 1.5 d). Loci of the 2:1 resonance with the second overtone and of the two half-integer resonances ($P_0/P_1 = 1.5$ and $P_0/P_5 = 3.5$) are also plotted. Triangles show the location of period-doubled models.

which the departure from this relation is observed and the maximum value of φ_{21} depend strongly on the luminosity. The correlation of the Fourier parameter progression with the P_2/P_0 ratio is lost if the Fourier parameters are plotted versus the period – see the blue curves in the right-hand panel of Fig. 14, which represent the same model sequences as plotted in Fig. 10. No doubt, the 2:1 resonance is crucial in shaping the progression of the radial velocity curves.

In Fig. 11 (right-hand panel), we plot the radial velocity curves along a sequence of $L = 25 L_{\odot}$. In contrast to Fig. 5, now a wide range of period ratios is probed, which clearly reveals the bump progression. The bump appears first in the middle of the ascending branch of the velocity curve, at the phase of maximum radius ($P_2/P_0 \approx 0.54$). Then, as period increases and period ratio decreases, the bump moves towards the phase of maximum expansion

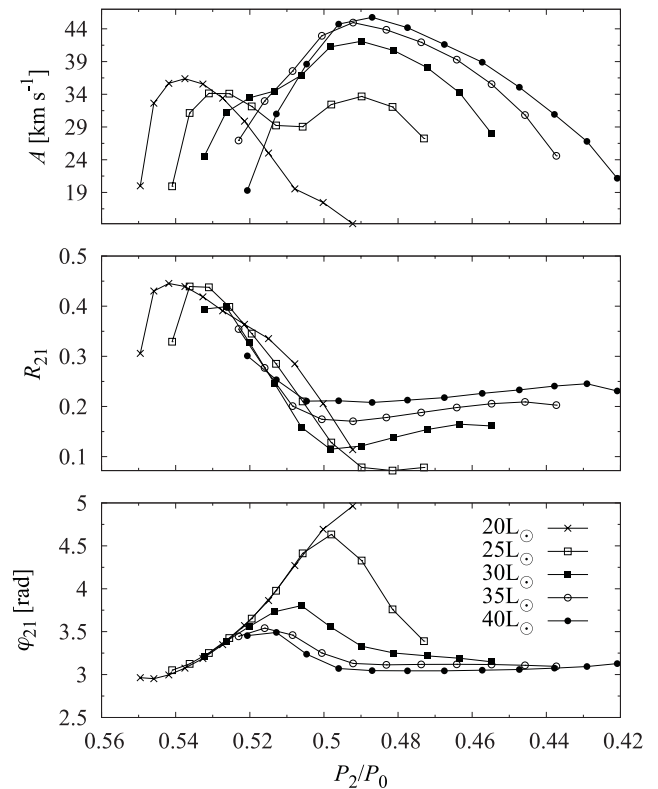


Figure 10. Peak-to-peak amplitude and the lowest order Fourier decomposition parameters for the radial velocity curves for $0.26 M_{\odot}$ models (set S1) of different luminosities (different symbols) plotted versus the linear P_2/P_0 period ratio. Pulsation period increases to the right.

velocity ($P_2/P_0 \approx 0.51$). For period ratios below ≈ 0.5 , the bump is present on the descending branch and disappears for $P_2/P_0 < 0.47$.

The bump progression is also visible for the *I*-band light curves (left-hand panel of Fig. 11), although in this case the interpretation is more difficult, because of additional features present in the light variation. At the highest effective temperature, the light curve is roughly triangular. A trace of bump appears on the descending branch, just after the maximum brightness, which next moves towards the ascending branch and deforms the brightness maximum. For effective temperatures below 6700 K ($P_2/P_0 < 0.52$), a pronounced bump is present on the ascending branch. It is present even for the lowest temperature model and, in general, is a feature of our models located in the centre and close to the red edge of the instability strip, even with period ratios as low as $P_2/P_0 \approx 0.44$ (not shown in Fig. 11), although it is much less pronounced in such models. It is likely that other non-resonant effects play a role in shaping this bump. Another feature of the light curves, well visible in Fig. 11, is a nearly flat and long phase of high brightness for cooler models ($T_{\text{eff}} \leq 6200 \text{ K}$). At the lowest effective temperatures, two brightness maxima at similar level are present. Origin of such shape is most likely non-resonant and connected to the development of extensive zone of efficient convective transfer at the phase of maximum compression, which is sustained then for nearly half the pulsation cycle.

Analysis of Figs 10 and 11 indicates that the 2:1 resonance influences the shape of the light and radial velocity curves in a wide range of period ratios, which we estimate to $0.47 < P_2/P_0 < 0.54$. The border values of P_2/P_0 are plotted with thin dotted lines in

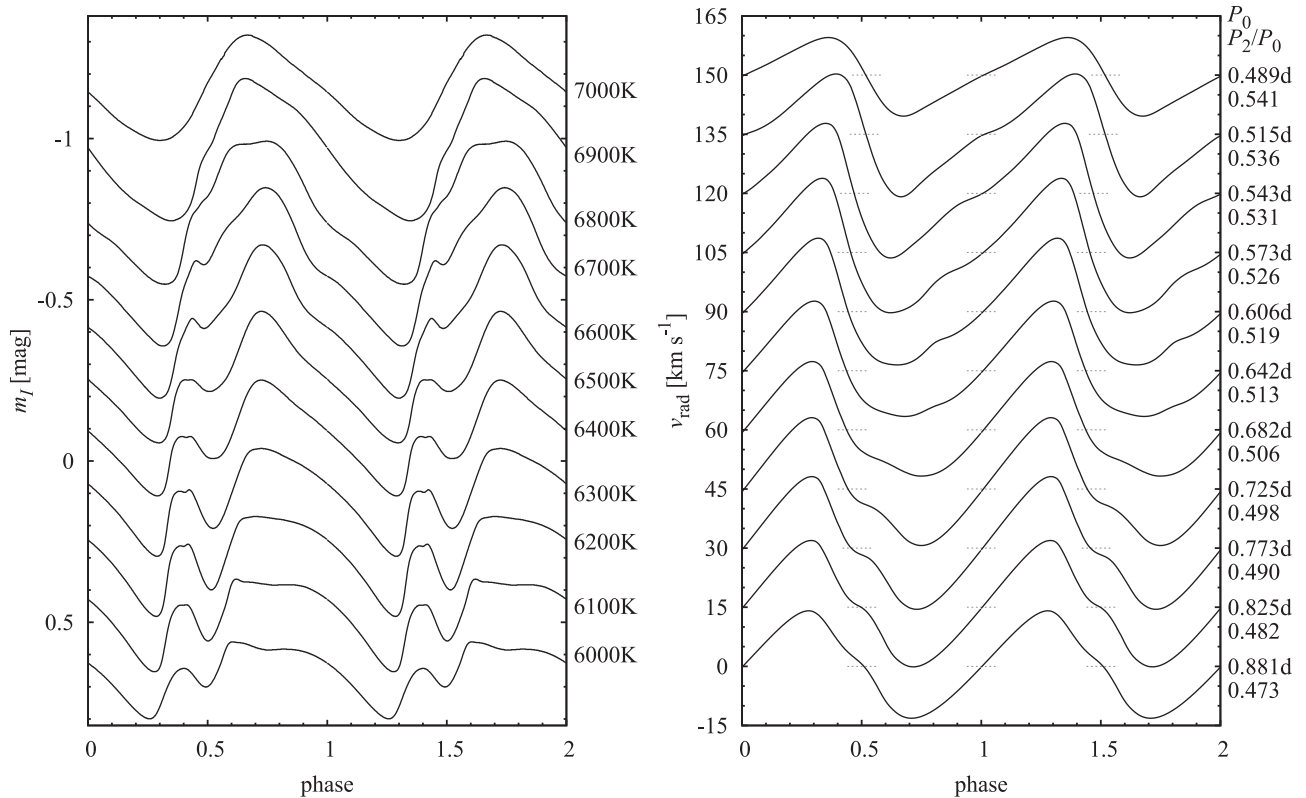


Figure 11. *I*-band light curves (left-hand panel) and radial velocity curves (right-hand panel) for hydrodynamic models of $0.26 M_{\odot}$ computed along a line of constant luminosity, $L = 25 L_{\odot}$. Models adopt convective parameters of set S1. Effective temperature is given on the right-hand side of the *I*-band curves, fundamental mode period and linear P_2/P_0 period ratio are given on the right-hand side of the velocity curves. For clarity, the consecutive light curves were shifted by 0.2 mag and radial velocity curves by 15 km s^{-1} . In the latter case, short horizontal line segments mark the zero velocity level. Velocity curves were scaled by constant projection factor, $p = 1.38$.

Fig. 9 and labelled with P_2/P_0 value. Clearly, the 2:1 resonance is influential in a significant part of the instability strip and hence is the most important effect shaping the light and radial velocity curves of BEPs.

Another resonant effect which we find in our models is a period-doubling effect. For some models, we observe alternating deep and shallow minima/maxima in the light and radial velocity variation – see Fig. 12 for exemplary light curves. Consequently, pulsation repeats after two fundamental mode periods. The behaviour is found only for some model sequences and is restricted to rather narrow parameter ranges. For models adopting convective parameters of

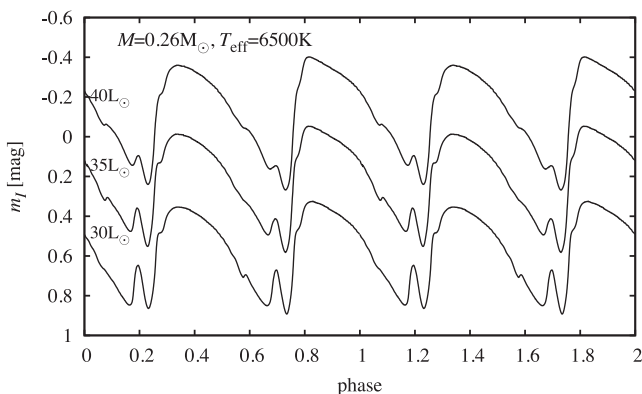


Figure 12. Exemplary *I*-band light curves for models with period-doubling effect.

set S1, period doubling was found only in the least massive, most luminous models. Their location is plotted with triangles in the top panel of Fig. 9.

As analysed by Moskalik & Buchler (1990), period doubling in the hydrodynamic models is caused by the half-integer resonances. The effect is observed in several types of large amplitude pulsators including RV Tau variables (caused by the 5:2 resonance, $P_0/P_2 = 2.5$; Moskalik & Buchler 1990), RR Lyr stars showing the Blazhko effect (caused by the 9:2 resonance, $P_0/P_9 = 4.5$; Szabó et al. 2010) and BL Her stars (caused by the 3:2 resonance, $P_0/P_1 = 1.5$; Smolec et al. 2012). In Fig. 9, we plot the loci of two half-integer resonances that might be influential in the case of BEPs models (red lines). These are the 3:2 resonance with the first overtone ($P_0/P_1 = 1.5$) and the 7:2 resonance with the fifth overtone ($P_0/P_5 = 3.5$). To cause the period doubling, the resonant overtone mode cannot be damped too strongly (Moskalik & Buchler 1990). This is the case for both resonances. The fifth overtone is a trapped envelope mode in the discussed models, for which the growth rate is high (Buchler & Kolláth 2001). Without the relaxation technique (e.g. Stellingwerf 1974), however, it is hard to identify which resonance is operational in these models. As the models are limited to narrow parameter ranges, we do not study this issue in more detail here.

We now turn to the discussion of the overall properties of the model light and radial velocity curves for BEPs, in terms of their Fourier decomposition parameters. To provide a feeling of how reliable our non-linear code is in predicting the Fourier parameters, and to provide a background for discussing the parameters of BEPs,

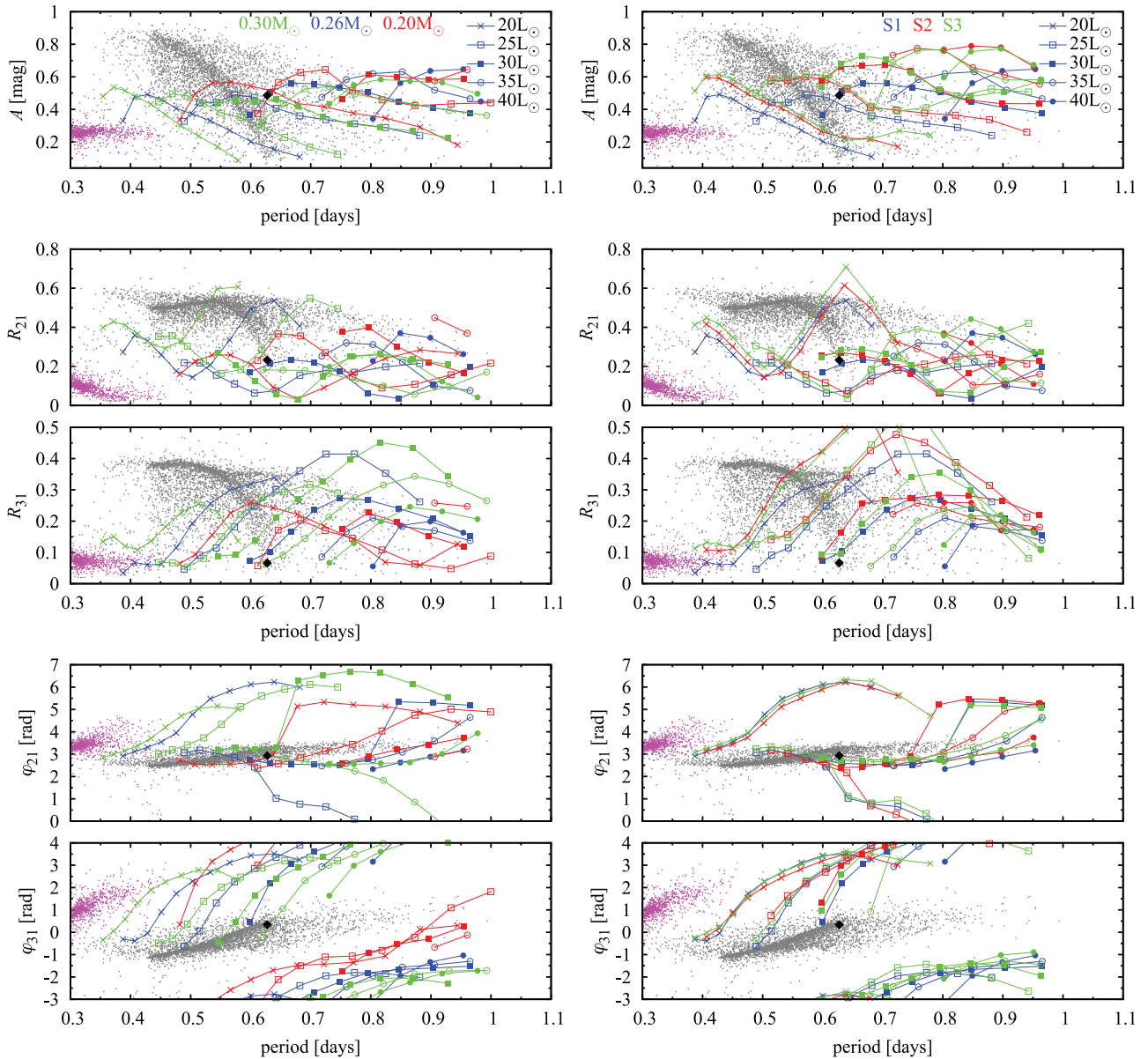


Figure 13. Fourier decomposition parameters for the I -band light curves of non-linear models of BEPs. Left-hand panel: models of different masses, 0.20, 0.26 and $0.30 M_{\odot}$, along five horizontal stripes with different luminosity (20–40 L_{\odot} , different symbols). Right-hand panel: models of $0.26 M_{\odot}$ and different luminosity and adopting different values of convective parameters (sets S1, S2 and S3). Diamond indicates the position of the BEP. For comparison, data for classical RR Lyrae stars from the Galactic bulge from the OGLE catalogue are plotted (grey dots for RRAb stars, magenta dots for RRC stars, each third plotted; Soszyński et al. 2011). Sine convention is used for Fourier phases.

we have conducted a model survey for classical RR Lyrae stars, briefly mentioned in Section 2, results of which were presented in Fig. 2. These models adopt the convective parameters of set S1, but results for other sets of convective parameters are very similar. Amplitude and R_{21} amplitude ratio are modelled satisfactorily, a somewhat too low values of R_{31} are predicted. Fourier phases agree well with the observations, indicating that majority of RR Lyrae stars have absolute luminosity around $50 L_{\odot}$.

Fourier parameters from similar survey of BEP models are plotted in Figs 13 (I -band light curves) and 14 (radial velocity curves) for all considered model sequences. Left-hand panels in these figures illustrate the effects of different mass of the models (with convective parameters of the models fixed to that of set S1), while right-hand panels illustrate the effects of using different convective parameters

in the modelling (sets S1, S2 and S3) while mass of the models is fixed to $0.26 M_{\odot}$. For each case, five model sequences with different absolute luminosities were computed. Successive models in each sequence were computed with a step of 100 K in effective temperature. The first, shortest period model in each sequence is the hottest model located at the direct proximity of the blue edge of the instability strip. It is clear that, with increasing luminosity, model sequences shift towards longer periods. In all the figures, we also mark the location of the BEP (diamond) and for the I -band light curves we also plot the location of RRAb and RRC (first overtone pulsators) stars from the Galactic bulge for a reference. Such comparison is not possible in the case of radial velocity parameters. Only for a few RR Lyrae stars, coverage of radial velocity curves is good enough to allow determination of their Fourier

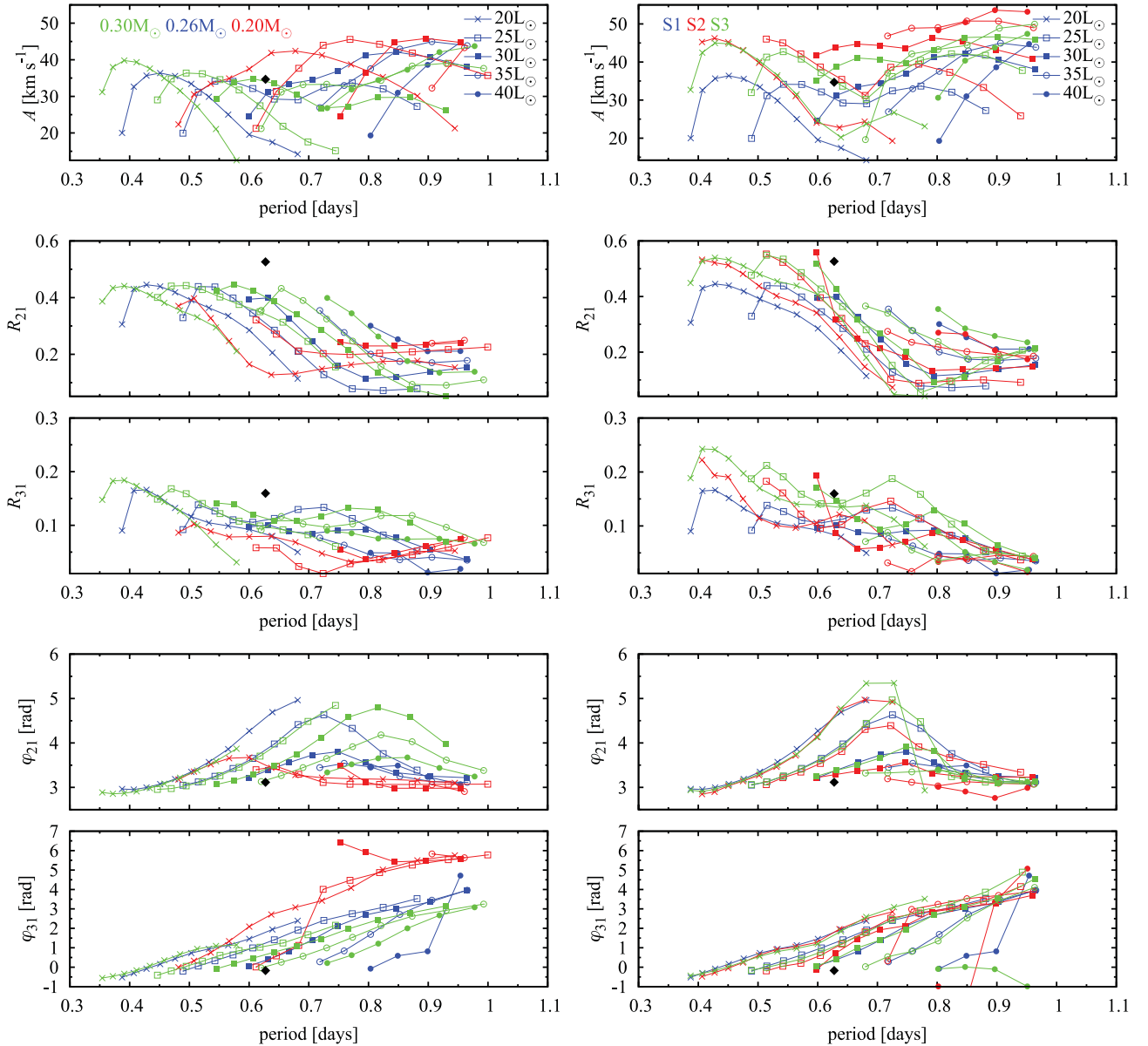


Figure 14. Fourier decomposition parameters for the radial velocity curves of non-linear models of BEPs. Left-hand panel: models of different masses, 0.20, 0.26 and $0.30 M_{\odot}$, along five stripes of different luminosity (20– $40 L_{\odot}$). Right-hand panel: models of $0.26 M_{\odot}$ and different luminosity and adopting different values of convective parameters (sets S1, S2 and S3). Diamond indicates the position of the BEP. Sine convention is used for Fourier phases.

parameters. Consequently, a meaningful comparison is not possible at the moment.

We first discuss the Fourier parameters for the *I*-band light curves displayed in Fig. 13. As discussed before, we expect that the 2:1 resonance will have a significant effect in shaping the light curves. We first note that progressions of Fourier parameters with pulsation period are very similar for different model sequences displayed in the figure. For example, the R_{21} progressions have a wavy shape with local minima in the middle and at the edges of the progression. R_{21} drops for the shortest and the longest period as a result of amplitude decrease at the edges of the instability strip. The decrease of R_{21} in the middle of the progression is a resonant effect (see Fig. 10). As resonance centre falls at different periods for different model sequences, the minimum of R_{21} also shifts in period. For example, for models with $M = 0.20 M_{\odot}$ the resonance centre is located at $P_0 \approx 0.6$ d for $20 L_{\odot}$ and at $P_0 \approx 1$ d for $40 L_{\odot}$ (top panel in Fig. 9).

The predicted peak-to-peak amplitudes of BEPs are below 0.6 mag in the *I* band, which is smaller than the typical amplitudes of RRab stars with periods shorter than ≈ 0.55 d. In this period range also the predicted amplitude ratios are smaller than in RRab stars. We note, however, that the predictions for amplitudes and amplitude ratios should be treated with caution. Amplitudes and consequently amplitude ratios strongly depend on the convective parameters adopted in the model, which is well visible if one compares the results for the models of sets S1 and S3 in the right-hand panel of Fig. 13. The lower the eddy viscosity (set S3), the higher the amplitudes and amplitude ratios become. Convective parameters should be calibrated to match the observational constraints, in particular the amplitude–period relation for a given group of pulsators. With only one BEP known at the moment, the calibration is necessarily very rough. Fortunately, the Fourier phases do not depend strongly on the pulsation amplitude, which is clear from the

analysis of the bottom-right panels of Figs 13 and 14. The Fourier phases depend only weakly on the adopted convective parameters as well. Thus, the Fourier phases are the best and most reliable predictions of our modelling.

The progressions for the Fourier phases (bottom panels of Fig. 13) are very interesting. Note that for φ_{31} the model sequences were plotted twice, shifted by 2π . The 2π ambiguity in the values of the Fourier phases should be kept in mind while analysing the figures. We note that φ_{21} progressions strongly depend on the mass and on the absolute luminosity adopted in the models. Thus, φ_{21} may provide useful constraints on the physical parameters of BEPs discovered in the future. Although for the majority of our models φ_{21} significantly differs from the RRab progression, values typical for RRab stars are also possible, particularly for models located on the hot side of the instability strip. Consequently, φ_{21} is not the best indicator of BEP. It is the φ_{31} Fourier phase that may be used to distinguish BEPs from RR Lyrae stars. Clearly, the values of φ_{31} predicted for BEPs differ significantly from the values typical for RR Lyrae stars. Only very close to the blue edge of the instability strip (and this is the case for the BEP) the values of φ_{31} are similar for the two groups. Through the majority of the instability strip φ_{31} is larger in the BEPs models. For cooler models, the φ_{31} value increases. In the middle of the instability strip, the difference between φ_{31} as predicted for BEPs and the RRab progression is around π rad. For lower masses, the difference becomes smaller, but even for $0.2 M_{\odot}$ models the difference is about 2 rad.

We also note that at shorter periods BEP models are also different from RRc stars. The predicted amplitudes are larger than those of RRc stars, and the same is true for the R_{21} ratio. The modelled Fourier phases, both φ_{21} and φ_{31} , fall in between the RRab and RRc progressions. The phases are larger than in RRab stars, but smaller than in RRc stars.

In the case of the radial velocity curves, the Fourier parameters displayed in Fig. 14 should be treated as predictions, to be compared with future observations of BEPs. It is hard to pinpoint the expected differences between the Fourier parameters for BEPs and those for RRab stars, as radial velocity observations of RRab stars are currently very scarce. The φ_{21} values seem to be the most interesting ones for radial velocity curves. They depend only slightly on the adopted convective parameters. The bell shape is a result of the bump progression, and this is the most important difference between BEPs and RRab stars. No bump progression is expected in the latter case. The presence of a bump on a radial velocity curve is thus a good indicator for a BEP. The situation is more difficult in the case of the light curves, as additional features (bumps, shoulders) which may result, for example, from the shock propagating in the atmosphere (e.g. Bono & Stellingwerf 1994) are commonly present in RRab stars. We also note that the φ_{21} values for the radial velocity curves might be used as an indicator of mass and absolute luminosity.

5 DISCUSSIONS AND CONCLUSIONS

In Section 3, we have conducted a model survey to reproduce the observed properties of the BEP. Our best model adopts the convective parameters of set S3 and a chemical composition typical for Population I stars, i.e. $X = 0.70$ and $Z = 0.01$. The model is located at the blue edge of the instability strip, its absolute luminosity is $33 L_{\odot}$ and effective temperature is $T_{\text{eff}} \approx 6970$ K. The model light curve fits the observed light variation very well. Good agreement was also obtained for the radial velocity curve (Fig. 8). We have reproduced the bump on the ascending branch of the radial velocity

curve of the BEP, and traced its origin to the 2:1 resonance between the fundamental mode and the second overtone, $P_2/P_0 = 0.5$.

The models with a chemical composition typical for Population II stars ($X = 0.76$) also reproduce the observations of the BEP well and have nearly the same luminosity and effective temperature. We note that although the mass of the BEP is very low and its pulsation resembles that of an RR Lyrae star, the BEP is the product of mass transfer in the binary system. 5.4 Gyr ago the progenitor of the BEP was a $1.4 M_{\odot}$ star, as models of Pietrzyński et al. (2012) indicate, and thus the chemical composition typical for Population I stars is very likely the correct one.

We also considered models with other values of convective parameters. The resulting properties of the best matching models for the BEP are then very similar to those quoted above (see Table 3) and therefore depend only slightly on the detailed treatment of convection in the model.

We note that the phase lag between the radial velocity curve and the light curve is systematically smaller in our models than that observed in the BEP. More computations are needed to find out how this discrepancy might be removed. The current models indicate that a slight helium enrichment might be needed. Also, effects of turbulent convection, not considered in this study (e.g. turbulent pressure, overshooting), need to be checked. A more detailed modelling of the BEP is planned in the near future.

The effective temperature of the BEP estimated by Pietrzyński et al. (2012) is ≈ 350 K larger ($T_{\text{eff}} = 7320 \pm 160$ K) than in our best matching model. Consequently, also the absolute luminosity is higher ($L = 46.2 \pm 9.3 L_{\odot}$). The estimates of effective temperature and absolute luminosity of the BEP not only differ from our results, but are also in conflict with stellar pulsation theory. They place the BEP outside the instability strip, as the analysis of Fig. 3 clearly indicates. This conclusion is independent of the convective parameters and chemical composition adopted in the model calculations.

The estimate of the effective temperature of the BEP by Pietrzyński et al. (2012) was based on the assumed $T_2 = 5000$ K effective temperature of the secondary component. It is a typical temperature for a $1.67 M_{\odot}$ giant, but it is not an actual measurement. Then, the effective temperature of the pulsating component of the binary was calculated using a temperature ratio ($T_1/T_2 = 1.464 \pm 0.010$) obtained from the analysis of the light curve of the binary. To check how the assumption on T_2 affects the results, we have redone the analysis of Pietrzyński et al. (2012) but adopting lower values of T_2 . It turned out that a decrease of T_2 by 100 K leads to a decrease of T_1 by ≈ 240 K. Thus, only a slight decrease of the effective temperature of the secondary component, by ≈ 150 K, brings the effective temperature of the BEP into agreement with the effective temperature resulting from our best models. The absolute luminosity is still somewhat too high ($L \approx 38 L_{\odot}$) as compared to our models, which is caused by slightly different estimates of the radius.

The radius of the BEP estimated by Pietrzyński et al. (2012) is $R = 4.24 \pm 0.24 R_{\odot}$ and, as we checked, is independent on the assumed value of T_2 . The values inferred from our models (see Fig. 3 and Table 3) are lower by up to 1.5σ (1.5σ for models with $Z = 0.01$ and 1.2σ for models with $Z = 0.001$). Multicolour photometry of the binary system may help us to determine the radius of the BEP more accurately and this way tell us how severe the discrepancy is.

We have conducted a large non-linear model survey for the new class of variable stars. The aim was to provide the criteria to distinguish BEPs from classical RR Lyrae pulsators. The resonant bump progression caused by the 2:1 resonance between the fundamental mode and the second overtone is the main factor expected to

determine the shapes of the light and radial velocity curves of BEPs. This is not the case for classical RR Lyrae stars. In the latter case, the 2:1 resonance falls close to the red edge of the instability strip and hence no bump progression is observed in classical RR Lyrae stars. Thus, the presence of a bump may indicate the binary evolution of the RR Lyrae impostor. We note that the location of the bump on the radial velocity curve is a measure of the P_2/P_0 ratio, which provides an excellent constraint on the stellar models. In the case of the light curves, one may expect pronounced bumps on the ascending branch, and long and flat or long and double-peaked phases of high brightness (Fig. 11). In some of our models with the lowest M/L ratio, we find a period-doubling effect (Fig. 12).

The other excellent discriminant of the new class of pulsating stars is the value of the φ_{31} Fourier phase for the I -band light curve. Except the models located extremely close to the blue edge of the instability strip, the expected values of φ_{31} differ significantly from the typical values for RRab stars. The values of φ_{21} , on the other hand, might be useful indicators of stellar mass and absolute luminosity. We also note that BEPs are expected to change (decrease) their periods very fast (Pietrzyński et al. 2012).

Our models clearly indicate that the BEP, with its light and radial velocity curves strongly mimicking the typical RR Lyrae curves, might be a rare case. For the majority of BEPs, significant departures from the observational properties of RR Lyrae stars are expected.

ACKNOWLEDGMENTS

We dedicate this paper to late Bohdan Paczynski ('Bep' to his Warsaw and Lick colleagues), a brilliant pioneer of stellar evolution within the confines of a Roche potential, and our colleague and mentor, who motivated many of us to take the difficult and challenging route of eclipsing binaries. We are grateful to Pawel Moskalik for helpful discussions and suggestions, reading and commenting the manuscript. Fruitful discussions with Wojciech Dziembowski are also acknowledged. We are grateful to the referee, Werner Weiss, for his helpful suggestions concerning the presentation of this paper. We gratefully acknowledge financial support for this work from the

Chilean Center for Astrophysics FONDAF 15010003, and from the BASAL Centro de Astrofísica y Tecnologías Afines (CATA) PFB-06/2007. Support from the Ideas Plus programme of Polish Ministry of Science and Higher Education, and the FOCUS and TEAM subsidies of the Foundation for Polish Science (FNP) is also acknowledged. KS acknowledges the financial support of the National Science Center through the grant DEC-2011/03/B/ST9/03299. Model computations presented in this paper were conducted on the psk computer cluster in the Copernicus Astronomical Centre, Warsaw, Poland.

REFERENCES

- Asplund M., Grevesse N., Sauval A. J., Allende Prieto C., Kiselman D., 2004, *A&A*, 417, 751
 Bono G., Stellingwerf R. F., 1994, *ApJS*, 93, 233
 Buchler J. R., Kolláth Z., 2001, *ApJ*, 555, 961
 Buchler J. R., Moskalik P., Kovács G., 1990, *ApJ*, 351, 617
 Fernley J., 1994, *A&A*, 284, L16
 For B.-Q. et al., 2010, *ApJ*, 708, 253
 Kovács G., Buchler J. R., 1989, *ApJ*, 346, 898
 Kuhfuß R., 1986, *A&A*, 160, 116
 Kurucz R. L., 2005, *Mem. Soc. Astron. Ital. Suppl.*, 8, 14
 Moskalik P., Bucher J. R., 1990, *ApJ*, 355, 590
 Ogloza W., Moskalik P., Kanbur S., 2000, in Szabados L., Kurtz D., eds, *ASP Conf. Ser. Vol. 203, The Impact of Large-Scale Surveys on Pulsating Star Research*. Astron. Soc. Pac., San Francisco, p. 235
 Pietrzyński G. et al., 2012, *Nat*, 484, 75
 Seaton M., 2005, *MNRAS*, 362, L1
 Simon N. R., 1984, *ApJ*, 284, 278
 Simon N. R., Schmidt E. G., 1976, *ApJ*, 205, 162
 Smolec R., Moskalik P., 2008, *Acta Astron.*, 58, 193
 Smolec R. et al., 2012, *MNRAS*, 419, 2407
 Soszyński I. et al., 2011, *Acta Astron.*, 61, 1
 Stellingwerf R. F., 1974, *ApJ*, 192, 139
 Stellingwerf R. F., 1982, *ApJ*, 262, 339
 Szabó R. et al., 2010, *MNRAS*, 409, 1244

This paper has been typeset from a $\text{\TeX}/\text{\LaTeX}$ file prepared by the author.